TECHNICAL PAPER

Improved disturbance rejection with online adaptive pole-zero compensation on a Φ-shaped PZT active suspension

**Chee Khiang Pang · Sai Cheong Tam · Guoxiao Guo ·
Ben M. Chen · Frank L. Lewis · Tong Heng Lee ·
Chunling Du**

Abstract In feedback control systems, the anti-resonant zeros cannot be arbitrarily placed, hence degrading tracking performance as well as input disturbance and noise rejection capabilities due to reduced gain at the frequencies of the zeros. In this paper, an online adaptive inverse control with saturation (OAICS) algorithm is proposed for compensating the minimum phase resonant poles and anti-resonant zeros of a PZT active suspension using measured position error signal. Experimental results on a Φ-shaped PZT active suspension using laser Doppler vibrometer (LDV) shows the proposed OAICS is effective in cancelling the first two dominant minimum phase pole-zero pairs to achieve high servo bandwidth and low sensitivity servo system with small overshoot during set-point tracking.

1 Introduction

With hungrier consumer demands for data storage capacities and faster access speeds, HDD industries are striving for increasing track densities coupled with higher spindle rotation speeds to make HDDs suitable for applications ranging from sitting in desktop computers to portable video recorders. These requirements of ultra-high and precise servo positioning accuracy translate directly into a high bandwidth and low sensitivity servo system, which is essential for ultra-strong disturbance and vibration rejection capabilities in the next generation of HDDs.

However, it is well known from control theory that the zeros of the plant to be controlled are not shifted by negative feedback while the closed-loop poles can be arbitrarily placed if the system is controllable (Chen et al. 2006). As such, the tracking performances and input disturbance rejection capabilities are deteriorated due to insufficient gain from filtering of the high frequency signals at the frequencies of the anti-resonant zeros by the retained zeros in the complementary sensitivity and shock transfer functions, respectively. Besides achieving a low-sensitivity servo system when anti-resonant zeros are compensated (Pang et al. 2005), common practices like using digital notch filters to compensate the resonant modes solely also cause a loss of phase margin, resulting in large overshoots during seek responses.

C. K. Pang (✉) · G. Guo · C. Du
A*STAR Data Storage Institute,
No. 5, Engineering Drive 1 (off Kent Ridge Crescent),
Singapore 117608, Republic of Singapore
e-mail: justinpang@nus.edu.sg

G. Guo
e-mail: GUO_Guoxiao@dsi.a-star.edu.sg

C. Du
e-mail: Du_Chunling@dsi.a-star.edu.sg

C. K. Pang · S. C. Tam · B. M. Chen · T. H. Lee
Department of Electrical and Computer Engineering,
National University of Singapore, 4 Engineering Drive 3,
Singapore 117576, Republic of Singapore

S. C. Tam
e-mail: sctam@nus.edu.sg

B. M. Chen
e-mail: bmchen@nus.edu.sg

T. H. Lee
e-mail: eleleeth@nus.edu.sg

F. L. Lewis
Automation and Robotics Research Institute,
The University of Texas at Arlington,
7300 Jack Newell Blvd. S., Fort Worth, TX 76118, USA
e-mail: lewis@uta.edu

As such, robust compensation of resonant pole and anti-resonant zero pairs using adaptive inverse control (AIC) is required. AIC has been studied extensively using the actual output of the channel (or plant) to update the inverse controller parameters of the finite impulse response (FIR) filter from signal processing (Farhang-Boroujeny 1998) and control theory (Widrow and Walach 1996) developments. While using FIR usually consists of long filter lengths, infinite impulse response (IIR) filters of lower orders have also been proposed to be effective in active noise control (ANC) signal processing problems which offer potential performance improvements coupled with less computational costs. Interested readers are referred to the algorithms in so-called (1) IIR-least means squares (IIR-LMS) in Feintuch (1976), (2) filtered-x LMS (FxLMS) (Bjarnason 1995) and the references therein, as well as (3) filtered-u LMS (FuLMS) (Eriksson et al. 1987; Mosquera et al. 1999; and the references therein for more details). The proofs for the FuLMS algorithm are also documented in Ljung (1977) and Wang and Ren (1999).

Similarly, adaptive parametric identification methodologies have also been studied and applied to HDD servo control to tackle the variations in natural frequencies and damping ratios of the actuators arising from different manufacturing batch processes, operating conditions, and read/write (R/W) head locations, etc. In Wu et al. (2000), the authors used a switch for adaptive identification of different PZT micro-actuators' resonant modes. The authors in Chow and Lawrence (2001) and Kang and Kim (2005) used adaptive estimators to identify and equalize the voice coil motor's (VCM) resonant modes in HDDs. However, it should be noted that the above-mentioned adaptive parametric identification methodologies are either performed offline, or "out-of" the servo control loop.

In this paper, an OAICS using measured PES is proposed to cancel the first two dominant minimum phase resonant pole and anti-resonant zero pairs online. The proposed OAICS has a robustness margin of up to ±10% to variations in actuators' natural frequencies, and can be extended to handle more pole-zero pairs on a proper choice of sampling rate to eradicate the non-minimum phase zeros (Åström et al. 1984). Our experiment results shows that a high servo bandwidth and low sensitivity servo system is achieved coupled with improvements in tracking performances of smaller overshoots from a larger phase margin, as compared to that using conventional resonant pole compensation with digital notch filters solely.

The rest of the paper is organized as follows. In the following parts, Sect. 2 describes the characteristics of the PZT active suspension envisaged for usage in dual-stage HDDs. Section 3 discusses and illustrates the effects of uncompensated anti-resonant zeros in feedback control systems. Section 4 proposes the OAICS with details on controller designs as well as parametric updates and selections. The performance of the proposed OAICS is verified with simulation and experimental results in Sect. 5. The conclusion and future work directions are summarized in Sect. 6.

2 Characteristics of PZT active suspension

To be appended on the VCM for dual-stage actuation (analogous to dual-stage mechanisms in optical recording technologies), the ideal PZT active suspension should be stiff (high damping for less resonant modes and parametric uncertainties) yet light (for achieving high servo bandwidth and faster disturbance rejection via error correction) simultaneously. Most PZT actuators exhibit pure gain behaviour at low frequencies coupled with high frequency minimum phase resonant poles and anti-resonant zeros. The picture of a Φ-shaped PZT active suspension fabricated by NHK Spring and its corresponding frequency response are shown in Figs. 1 and 2, respectively.

It can be seen from Fig. 2 that the PZT active suspension have numerous high frequency anti-resonant zeros. As such, the tracking and input disturbance rejection capabilities of the PZT active suspension at the frequencies of the these zeros will be greatly reduced as the gain is highly attenuated, causing performance deterioration as the actuator is unable to "reach" those frequencies for necessary error rejection.

From Fig. 2, it can be seen that the Φ-shaped PZT active suspension has resonant poles at 6.05, 10.0, 16.8, 32.5, and 41.5 kHz, as well as anti-resonant zeros at 7.25, 13.0, 25.0, 38.0, and 50.0 kHz. The identified mathematical model $P(s)$ of the frequency response of the PZT active suspension is given by
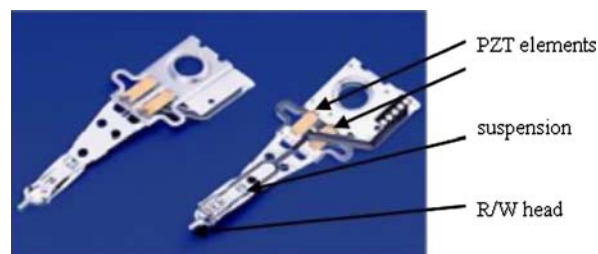

Fig. 1 Picture of a Φ-shaped PZT active suspension (NHK Spring). The R/W head is displaced in the in-plane direction when the PZT elements arranged in a push-pull configuration are subjected to voltage or charge actuation
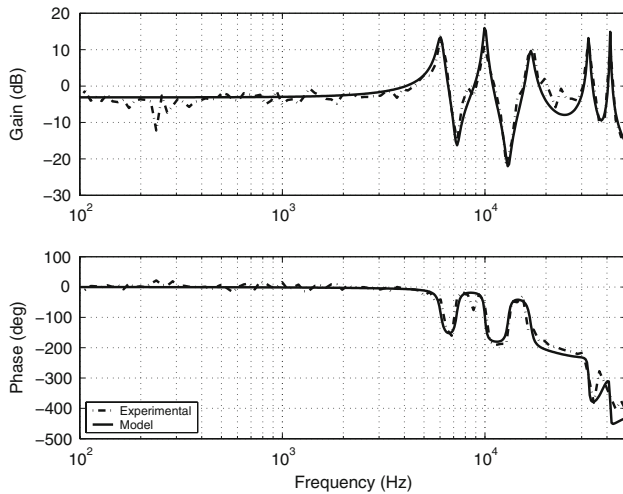
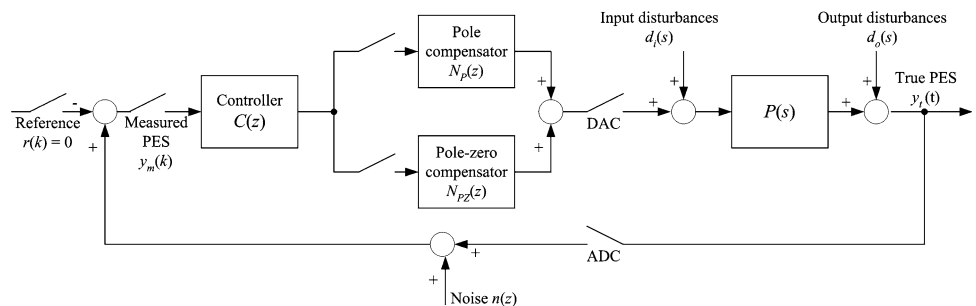**Fig. 2** Frequency response of a Φ-shaped PZT active suspension

$$P(s) = 0.0656 \times \frac{s^2 + 2(0.0275)(2\pi 7.25 \times 10^3) + (2\pi 7.25 \times 10^3)^2}{s^2 + 2(0.0325)(2\pi 6.05 \times 10^3) + (2\pi 6.05 \times 10^3)} \cdots$$
$$\times \frac{s^2 + 2(0.025)(2\pi 13.0 \times 10^3) + (2\pi 13.0 \times 10^3)^2}{s^2 + 2(0.0175)(2\pi 10.0 \times 10^3) + (2\pi 10.0 \times 10^3)} \cdots$$
$$\times \frac{s^2 - 2(0.5)(2\pi 25.0 \times 10^3) + (2\pi 25.0 \times 10^3)^2}{s^2 + 2(0.03)(2\pi 16.8 \times 10^3) + (2\pi 16.8 \times 10^3)^2} \cdots$$
$$\times \frac{s^2 + 2(0.09)(2\pi 38.0 \times 10^3) + (2\pi 38.0 \times 10^3)^2}{s^2 + 2(0.01)(2\pi 32.5 \times 10^3) + (2\pi 32.5 \times 10^3)^2} \cdots$$
$$\times \frac{s^2 + 2(0.5)(2\pi 50.0 \times 10^3) + (2\pi 50.0 \times 10^3)^2}{s^2 + 2(0.0045)(2\pi 41.5 \times 10^3) + (2\pi 41.5 \times 10^3)^2} \quad (1)$$

It should be noted that except for the anti-resonant zero at 25.0 kHz, the rest of the resonant poles and anti-resonant zeros are of minimum phase.

3 Effects of uncompensated anti-resonant zeros

In this section, the effects of uncompensated anti-resonant zeros are illustrated with a simulation example. The simulation block diagram to illustrate the effects of uncompensated anti-resonant zeros is shown in Fig. 3.

3.1 Controller design

For our simulations, a sampling frequency f_s of 100 Hz is used to capture most of the modelled dynamics of the Φ-shaped PZT active suspension. The designs of the digital pole compensator $N_P(z)$, pole-zero compensator $N_{PZ}(z)$, and feedback controller $C(z)$ shown in Fig. 3 are detailed in this section.

3.1.1 Pole compensator $N_P(z)$

In pole compensator, the small damping ratios of all the five resonant modes are replaced with unity to attenuate the gain of the control signal and hence prevent excitation of the corresponding resonant pole. As such, $N_P(s)$ is given by

$$N_P(s) = \frac{s^2 + 2(0.0325)(2\pi 6.05 \times 10^3) + (2\pi 6.05 \times 10^3)}{s^2 + 2(1)(2\pi 6.05 \times 10^3) + (2\pi 6.05 \times 10^3)} \cdots$$
$$\times \frac{s^2 + 2(0.0175)(2\pi 10.0 \times 10^3) + (2\pi 10.0 \times 10^3)}{s^2 + 2(1)(2\pi 10.0 \times 10^3) + (2\pi 10.0 \times 10^3)} \cdots$$
$$\times \frac{s^2 + 2(0.03)(2\pi 16.8 \times 10^3) + (2\pi 16.8 \times 10^3)^2}{s^2 + 2(1)(2\pi 16.8 \times 10^3) + (2\pi 16.8 \times 10^3)^2} \cdots$$
$$\times \frac{s^2 + 2(0.01)(2\pi 32.5 \times 10^3) + (2\pi 32.5 \times 10^3)^2}{s^2 + 2(1)(2\pi 32.5 \times 10^3) + (2\pi 32.5 \times 10^3)^2} \cdots$$
$$\times \frac{s^2 + 2(0.0045)(2\pi 41.5 \times 10^3) + (2\pi 41.5 \times 10^3)^2}{s^2 + 2(1)(2\pi 41.5 \times 10^3) + (2\pi 41.5 \times 10^3)^2}$$
$$(2)$$

and $N_P(z)$ can then be obtained by discretizing $N_P(s)$ at f_s using pole-zero matching.

3.1.2 Pole-zero compensator $N_{PZ}(z)$

In the pole zero compensator, the high frequency resonant pole and anti-resonant zero pairs are inverted directly for inverse control. As for the non-minimum phase zero at 25.0 kHz, the negative damping ratio is replaced by its positive counterpart. While the gain will be perfectly compensated, the phase will be negated and hence an unavoidable phase loss will occur at 25.0 kHz.

Fig. 3 Simulation block diagram to illustrate pole compensation using digital notch filters in $N_P(z)$ and pole-zero compensation with approximate digital inverse filters in $N_{PZ}(z)$

As such, $N_{PZ}(s)$ is given by

$$N_{PZ}(s) = \frac{s^2+2(0.0325)(2\pi 6.05\times 10^3)+(2\pi 6.05\times 10^3)}{s^2+2(0.0275)(2\pi 7.25\times 10^3)+(2\pi 7.25\times 10^3)^2}\cdots$$
$$\times\frac{s^2+2(0.0175)(2\pi 10.0\times 10^3)+(2\pi 10.0\times 10^3)}{s^2+2(0.025)(2\pi 13.0\times 10^3)+(2\pi 13.0\times 10^3)^2}\cdots$$
$$\times\frac{s^2+2(0.03)(2\pi 16.8\times 10^3)+(2\pi 16.8\times 10^3)^2}{s^2+2(0.5)(2\pi 25.0\times 10^3)+(2\pi 25.0\times 10^3)^2}\cdots$$
$$\times\frac{s^2+2(0.01)(2\pi 32.5\times 10^3)+(2\pi 32.5\times 10^3)^2}{s^2+2(0.09)(2\pi 38.0\times 10^3)+(2\pi 38.0\times 10^3)^2}\cdots$$
$$\times\frac{s^2+2(0.0045)(2\pi 41.5\times 10^3)+(2\pi 41.5\times 10^3)^2}{s^2+2(0.5)(2\pi 50.0\times 10^3)+(2\pi 50.0\times 10^3)^2}$$

(3)

and $N_{PZ}(z)$ can then be obtained by discretizing $N_{PZ}(z)$ at f_s using pole-zero matching.

3.1.3 Feedback controller C(z)

To ensure a low positive sensitivity while retaining a high servo bandwidth (Pang et al. 2005), the feedback controller $C(s)$ is designed as a proportional-integral (PI) controller as

$$C(s) = K_C\frac{s+\pi f_s}{s+2\pi 0}$$

(4)

where K_C can be found with the relation $|C(j2\pi f_C)N_P(j2\pi f_C)P(j2\pi f_C)| = 1$ or $|C(j2\pi f_C)N_{PZ}(j2\pi f_C)P(j2\pi f_C)| = 1$ for pole compensator $N_P(s)$ or pole-zero compensator $N_{PZ}(s)$, respectively, with f_C as the open loop gain crossover frequency set at 1 kHz. $C(z)$ is then obtained by discretizing $C(s)$ at f_s using bilinear transformation.
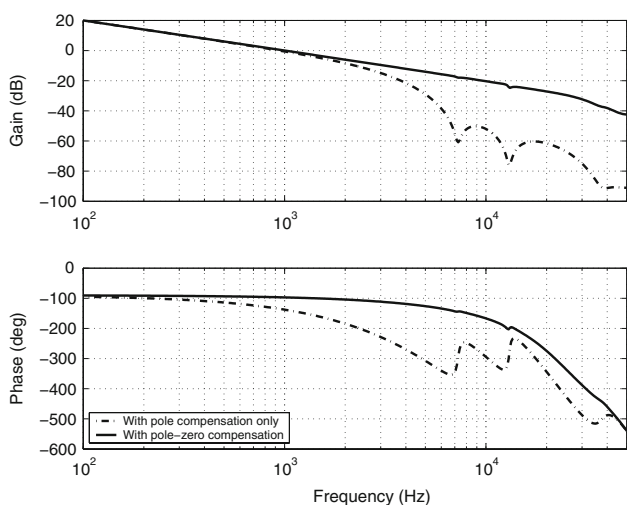
3.2 Frequency responses

The frequency response of the simulated open loop transfer functions with pole compensation and that with pole-zero compensation are shown in Fig. 4.

From Fig. 4, it can be seen that the the open loop transfer function using pole-zero compensation with $N_{PZ}(z)$ has a smaller relative degree and roll-off at high frequencies. This effective lower the inertia of the Φ-shaped PZT active suspension, resulting in a faster response from the closed-loop system.

Also, it can be seen from Fig. 4 that a large phase loss is incurred when using digital notch filters in pole compensator $N_P(z)$ solely. This translates directly to a reduced phase margin, coupled with poorer transient responses from large overshoots during seek responses. However for brevity in comparison purposes but without loss of generality, a conservative gain crossover frequency of 1 kHz is chosen for both servo systems. It is worth noting that a higher gain crossover frequency for that using pole-zero compensation can be achieved due to a smaller phase loss.

The frequency response of the simulated complementary sensitivity transfer functions T and sensitivity transfer functions S, with pole compensator $N_P(z)$ and that with pole-zero compensator $N_{PZ}(z)$ are shown in Fig. 5.

At the same crossover frequency of 1 kHz, the sensitivity transfer function error rejection range improves from 600 Hz using pole compensator $N_P(z)$ to 1.8 kHz with pole-zero compensator $N_{PZ}(z)$. Also, a low positive sensitivity is obtained to prevent amplification of output disturbances at frequencies where feedback control is degrading servo performance (Pang et al. 2005).
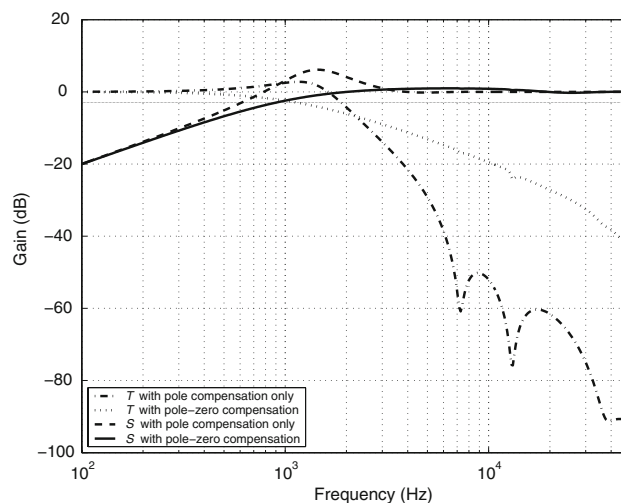

Fig. 4 Frequency responses of simulated open loop transfer functions. *Dashed-dot* with pole compensation only. *Solid* with pole-zero compensation

Fig. 5 Frequency responses of simulated sensitivity transfer functions. *Dashed-dot T* with pole compensator $N_P(z)$. *Dotted T* with pole-zero compensator $N_{PZ}(z)$. *Dashed S* with pole compensator $N_P(z)$. *Solid S* with pole-zero compensator $N_{PZ}(z)$

From the simulated complimentary sensitivity transfer functions shown in Fig. 5, a higher tracking gain is attained from a lower roll-off at high frequencies, especially those at the frequencies of the uncompensated anti-resonant zeros. The reduced inertia hence improves tracking performance during seek responses with more high frequency components. Although the closed-loop bandwidth is smaller when using pole-zero compensator $N_{PZ}(z)$, it should be noted that a much higher closed-loop bandwidth (corresponding to higher open loop gain crossover frequency) can be achieved, but is maintained at the same crossover frequency of 1 kHz for comparison purposes but without loss of generality.

3.3 Time responses

To further illustrate the advantages of anti-resonant zero compensation using pole-zero compensator $N_{PZ}(z)$, simulations of track-seeking responses in time domain are carried out. The step response of 1 μm is shown in Fig. 6.
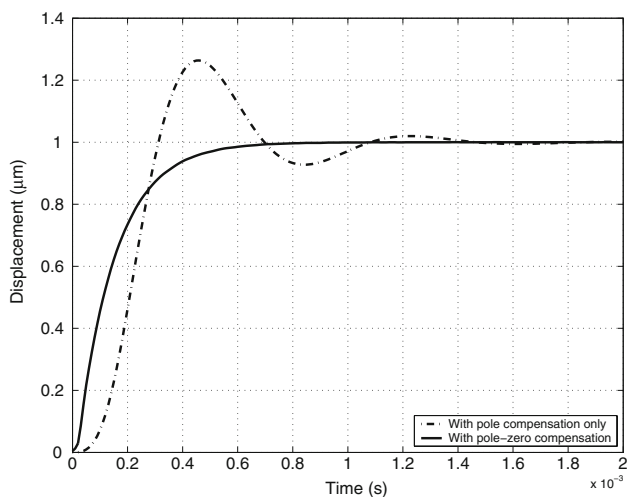

Fig. 6 Step responses. *Dashed-dot* with pole compensation only. *Solid* with pole-zero compensation

From Fig. 6, it can be the inclusion of high frequency signals at the frequencies of the anti-resonant zeros at 7.25, 13.0, 25.0, 38.0, and 50.0 kHz causes a faster transient response at from 0 to 0.3 ms. Due to a healthier phase margin when compared to that using digital notch filters for pole compensation solely, the overshoots and undershoots are removed for better seek to settle transitions with less induced oscillations and faster settling.

4 Online adaptive inverse control with saturation

To tackle the problem of unshifted anti-resonant zeros in feedback control systems and their effects mentioned in Sect. 3, an OAICS is proposed to adaptively cancel the minimum phase anti-resonant zeros and resonant poles with manufacturing tolerances and robustness considerations. The block diagram of the proposed OAICS system is shown in Fig. 7.

The main motivation of the proposed OAICS is to use the plant inverse compensator $\tilde{P}^{-1}(z)$ to compensate for the minimum phase resonant pole and anti-resonant zero pairs, and is updated adaptively from the error signals $e(k)$ via comparisons with the measured PES $y_m(k)$ and the estimated PES output $y_e(k)$ using the discretized plant model $\hat{P}(z)$ constructed earlier. $C(z)$ is the feedback controller which constructs the desired open loop shape, and compensates for any resonant modes which are not to be considered for inverse pole-zero compensation by $\tilde{P}^{-1}(z)$ to ensure closed-loop stability.

The components in the proposed OAICS and their design specifications are further detailed in this section.

4.1 Feedback controller $C(z)$

To ensure a low sensitivity while retaining a high bandwidth, the feedback controller $C(s)$ is designed according to the guidelines in Pang et al. (2005) to be

Fig. 7 Block diagram of proposed OAICS algorithm with anti-windup compensator $W(z)$ to prevent control signal or actuator saturation
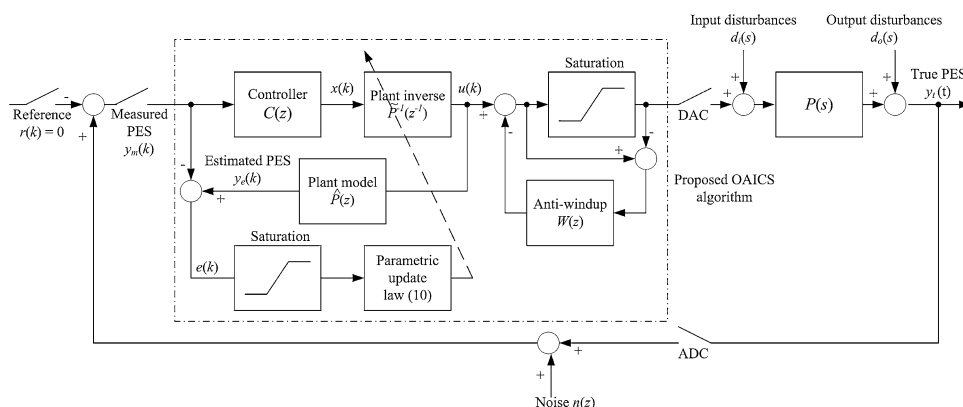
$$C(s) = K_C \frac{s + 2\pi f_s}{s + 2\pi \frac{f_C}{g_C}}$$

$$\times \frac{s^2 + 2(0.03)(2\pi16.8 \times 10^3) + (2\pi16.8 \times 10^3)^2}{s^2 + 2(1)(2\pi16.8 \times 10^3) + (2\pi16.8 \times 10^3)^2} \cdots$$

$$\times \frac{s^2 + 2(0.01)(2\pi32.5 \times 10^3) + (2\pi32.5 \times 10^3)^2}{s^2 + 2(1)(2\pi32.5 \times 10^3) + (2\pi32.5 \times 10^3)^2} \quad (5)$$

which in essence is a first order lag cascaded two digital notch filters at 16.8 kHz and 32.5 kHz to increase the damping ratios of the corresponding resonant poles to unity. A $g_C = 2$ is used and f_C is the open loop gain crossover frequency set at 2 kHz and K_C can be found with the relation $|C(j2\pi f_C) P(j2\pi f_C)| = 1$. The minimum phase resonant pole at 41.5 kHz and anti-resonant zero at 50.0 kHz are not compensated due to its distance from the gain crossover frequency at 2 kHz which will not affect closed-loop stability.

$C(z)$ can then be obtained by discretizing $C(s)$ at f_s of 100 kHz using pole-zero matching.

4.2 Plant model $\hat{P}(z)$

Converting $P(s)$ in Eq. 1 to z-domain via Zero-Order Hold (ZOH) equivalence at a sampling frequency f_s of 100 kHz, the transfer function of the discretized plant $\hat{P}(z)$ can be obtained. With the discrete model of plant $P(z)$ known, the plant model $\hat{P}(z)$ shown in Fig. 7 can be realized. The outputs of $\hat{P}(z)$ can also be measured via a 'hard' sensor (Pang et al. 2006) or a 'soft' sensor (Pang et al. 2007a).

4.3 Nominal plant inverse compensator $\tilde{P}^{-1}(z^{-1})$

If the plant to be controlled is composed of minimum phase resonant poles and anti-resonant zeros solely (ideally), all the pole-zero pairs will be considered and included into $\tilde{P}^{-1}(z^{-1})$ for inverse compensation. However for our application, only the first two dominant minimum phase resonant pole and anti-resonant zero pairs are chosen for adaptive pole-zero compensation for illustration but without loss of generality, due to the existence of a non-minimum phase zero at 25.0 kHz as can be seen in Eq. 1. It should be noted that a suitable sampling frequency can be chosen as stipulated by the guidelines in Åström et al. (1984) to remove the non-minimum behaviour of the corresponding anti-resonant zeros.

Rewriting the plant model $\hat{P}(z)$ in discrete filter form as

$$\hat{P}(z^{-1}) = \frac{1 + \sum_{j=1}^{2M} b_j z^{-j}}{\sum_{i=0}^{2M} a_i z^{-i}} \quad (6)$$

where M is the number of resonant pole and anti-resonant zero pairs. b_j and a_i are the normalized coefficients of the stable anti-resonant zero and resonant pole polynomials written in discrete filter form up to frequencies of interest, respectively.

The nominal digital plant inverse compensator $\tilde{P}^{-1}(z^{-1})$ can then be written as

$$\tilde{P}^{-1}(z^{-1}) = \frac{\sum_{i=0}^{2M} a_i z^{-i}}{1 + \sum_{j=1}^{2M} b_j z^{-j}}$$

$$= \frac{U(z)}{X(z)} \quad (7)$$

and the output of $\tilde{P}^{-1}(z^{-1})$ at sample instant k can be written in time series and closed-form as

$$u(k) = \sum_{i=0}^{2M} a_i(k)x(k-i) - \sum_{j=1}^{2M} b_j(k)u(k-j)$$

$$= \mathbf{a}^T(k)\mathbf{x}(k) + \mathbf{b}^T(k)\mathbf{u}(k-1) \quad (8)$$

where $\mathbf{x}(k) = [x(k) \quad x(k-1)\ldots x(k-2M)]^T$ is a vector of input sequence data to the nominal plant inverse $\tilde{P}^{-1}(z^{-1})$, which in essence is a vector of filtered PES from feedback controller $C(z)$ analogous to the FuLMS framework. $\mathbf{u}(k-1) = [u(k-1) \quad u(k-2)\ldots u(k-2M)]^T$ is a vector of past outputs of $\tilde{P}^{-1}(z^{-1})$ which constitutes the IIR. $\mathbf{a}(k) = [a_0(k) \quad a_1(k)\ldots a_{2M}(k)]^T$ and $\mathbf{b}(k) = [b_1(k) \quad b_2(k)\ldots b_{2M}(k)]^T$ are vectors of the coefficients of the stable anti-resonant zero and resonant pole polynomials, respectively, with $\mathbf{a}(0)$ and $\mathbf{b}(0)$ are initialized to the nominal coefficients of $\tilde{P}^{-1}(z^{-1})$.

It is worth noting that elements $\mathbf{x}(k)$ and $\mathbf{u}(k-1)$ contain past realizable signals required for initialization of the IIR.

4.4 Parametric updates

In the proposed OAICS system shown in Fig. 7, filtered PES by feedback controller $C(z)$ is used which is analogous to many ANC problems where only filtered error is available.

Let $\mathbf{w}(N) = [\mathbf{a}^T(N) \quad \mathbf{b}^T(N)]^T$ and $\mathbf{h}(N) = [\mathbf{x}^T(N) \quad \mathbf{u}^T(N-1)]^T$ with N being the updating instants. $\bar{e}(N)$ is the stochastic mean of $e(N)$ from previous updating instant $N-1$ till current update instant N (or error between estimated PES $y_e(N)$ and measured PES $y_m(N)$ as can be seen from Fig. 7), and $\bar{e}(N)$ should ideally be zero after parametric convergence.

Defining the saturation function $\mathrm{sat}(.)$ as

$$\mathrm{sat}(\psi) = \mathrm{sign}(\psi) \min\{\bar{\psi}, |\psi|\} \quad (9)$$

where $\bar{\psi}$ denotes the ceiling and $|\psi|$ is the absolute value of ψ, respectively, the convergence of the closed-loop stability using the proposed OAICS system is discussed and proven below.

Theorem 1 *The proposed OAICS algorithm is stable and the open loop transfer function converges to the feedback*

controller $C(z)$ using the following modified LMS parametric update law with saturation considerations

$$\mathbf{w}(N+1) = \mathbf{w}(N) - 2\mu\, sat[\bar{e}(N)]\mathbf{h}(N) \qquad (10)$$

if

$$\mu < \frac{1}{\rho(N)|\mathbf{h}(N)|^2} \qquad (11)$$

where μ is a small positive learning rate scalar and $\rho(N) = \frac{sat[\bar{e}(N)]}{\bar{e}(N)}$.

Assumption 1 Parametric adjustments are terminated and not executed when $\mu = 0$.

Assumption 2 The variations of the controller parameters are small at updating instants N, i.e. $\mathbf{h}(N+1) \approx \mathbf{h}(N)$ which is valid if the nominal plant inverse compensator $\tilde{P}^{-1}(z^{-1})$ has already been initialized to the corresponding coefficients of the identified values to ensure stability of the closed-loop system before beginning the adaptive parametric updating process using Eq. 10. Moreover, the digital coefficients are typically of small magnitudes (less than two) when compared to their analogue counterparts which are in typical orders of powers of ten, hence resulting in numerical adjustments of small magnitudes in the coefficients of $\mathbf{h}(N)$. This ensures convergence to the local minimum in a small vicinity to be verified and explored in Sect. 5.1.

Proof 1 For a suitable choice of parametric adjustment gain or learning rate μ, consider the following positive definite Lyapunov candidate $V(N)$

$$V(N) = \frac{1}{2}\bar{e}^2(N) > 0, \qquad \forall N \qquad (12)$$

As such, the difference of $V(N)$ at successive instants N can be written as $\Delta V(N)$ where

$$\begin{aligned}\Delta V(N) &= V(N+1) - V(N)\\ &= \frac{1}{2}\left[\bar{e}^2(N+1) - \bar{e}^2(N)\right]\\ &= \Delta\bar{e}(N)\left[\frac{1}{2}\Delta\bar{e}(N) + \bar{e}(N)\right]\end{aligned} \qquad (13)$$

Similarly, the difference in $\bar{e}(N)$ at successive instants N can also be written as $\Delta\bar{e}(N)$ where

$$\begin{aligned}\Delta\bar{e}(N) &= \bar{e}(N+1) - \bar{e}(N)\\ &= -E[y_m(N+1)] + E[y_e(N+1)] + E[y_m(N)]\\ &\quad - E[y_e(N)]\\ &= \mathbf{w}^T(N+1)\mathbf{h}(N+1) - \mathbf{w}^T(N)\mathbf{h}(N)\\ &\approx \left[\mathbf{w}^T(N+1) - \mathbf{w}^T(N)\right]\mathbf{h}(N)\\ &= \Delta\mathbf{w}^T(N)\mathbf{h}(N)\end{aligned} \qquad (14)$$

with zero reference during track-following control in HDDs, as well as assuming that the measured PES sequence $y_m(k)$ is of zero mean and stationary, i.e. $E[y_m(N+1)] = E[y_m(N)] = 0$ with $E(\cdot)$ being the expectation operator.

From Eq. 10, the difference $\Delta\mathbf{w}(N)$ of $\mathbf{w}(N)$ at successive instants N can be written as

$$\Delta\mathbf{w}(N) = -2\mu\, sat[\bar{e}(N)]\mathbf{h}(N) \qquad (15)$$

and combining with Eq. 14, we get

$$\begin{aligned}\Delta\bar{e}(N) &= -2\mu\, sat[\bar{e}(N)]\mathbf{h}^T(N)\mathbf{h}(N)\\ &= -2\mu\, sat[\bar{e}(N)]|\mathbf{h}(N)|^2\end{aligned} \qquad (16)$$

Therefore substituting Eq. 16 into Eq. 13 gives

$$\begin{aligned}\Delta V(N) &= -2\mu\, sat[\bar{e}(N)]|\mathbf{h}(N)|^2\left\{-\mu\, sat[\bar{e}(N)]|\mathbf{h}(N)|^2 + \bar{e}(N)\right\}\\ &= -2\mu\, sat[\bar{e}(N)]\bar{e}(N)|\mathbf{h}(N)|^2\left\{-\mu\rho(N)|\mathbf{h}(N)|^2 + 1\right\}\end{aligned} \qquad (17)$$

where $\rho(N) = \frac{sat[e(N)]}{e(N)}$ which is positive for all N if $e(N) \neq 0$. This condition is ensured as parametric updating will not be executed as explained earlier in Eq. 10.

Since $sat[\bar{e}(N)]\bar{e}(N) > 0$ for all $\bar{e}(N) \neq 0$, the term in $\{\cdot\}$ of Eq. 17 must be positive definite for all N for a negative definite $\Delta V(N)$

$$\begin{aligned}&-\mu\rho(N)|\mathbf{h}(N)|^2 + 1 > 0\\ &\mu < \frac{1}{\rho(N)|\mathbf{h}(N)|^2}\end{aligned} \qquad (18)$$

and the value of μ chosen will ensure the required parametric convergence.□

Remark 1 μ can also be chosen as a time-varying gain $\mu(N)$ according to the relationship in Eq. 18.

Remark 2 The saturation function is included in the parametric update law in Eq. 10 to avoid large adjustments which causes poles to drift outside the unit disc during large impulse shock disturbances.

Remark 3 It is also worth noting that a Repeatable Run-Out (RRO) estimator can be included for removing the periodic repeatable components to prevent the parameters which being trapped in a local optimum. Interested readers are kindly referred to Pang et al. (2007b) for an example of such an online RRO estimator.

4.5 Anti-windup compensator $W(z)$

As the PZT active suspensions are manufactured to move in small displacements (typically in orders of nm), saturation of the actuators and integrators in the controllers might occur during short-span seeks which destabilizes the closed-loop servo system. Also, PZT elements used for actuating the PZT active suspension are also known to have "creep" effects or DC drifts, which cause the true

displacement of the PZT actuators to diverge from the desired setpoint slowly. As such to prevent the saturation of the PZT actuators, a simple anti-windup compensator $W(z)$ of the form is included

$$W(z) = \alpha z^{-1} \tag{19}$$

with $0 < \alpha \leq 1$ to safeguard against instability from large actuation. The induced oscillations during parametric adaptations from control signal saturation during seek operations are greatly reduced.

5 Performance analysis

In this section, the proposed OAICS is evaluated with simulation studies and experimental implementations on the so-called Φ-shaped PZT active suspension as shown earlier in Fig. 2.

5.1 Simulation studies

For our application, μ is chosen as a static scalar of 2.5×10^{-4} and $M = 2$ to compensate for the first two dominant pairs of minimum phase resonant poles and anti-resonant zeros. Parametric updates are done at at after every ten samples of of measurement, i.e. $N = 10l/f_s$ where l is an integer. The identified vibration model and noise sources model reported in Du et al. (2002) with a Fujitsu fluid bearing spindle motor HDD rotating at 5400 rpm is used to emulate input disturbances d_i, output disturbances d_o, and noise n.

To demonstrate the convergence and robustness of the OAICS to different operating locations from different R/W heads, environmental temperatures, locations on disk, etc.,
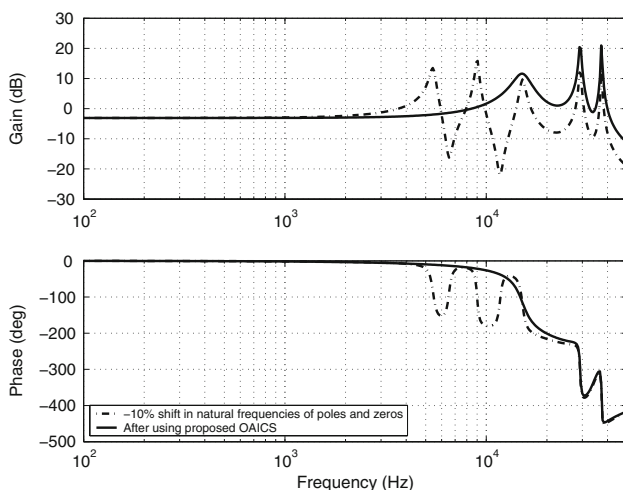

Fig. 8 Frequency response of $\tilde{P}^{-1}(z^{-1})P(z)$ with frequency variations of -10% in the first two resonant pole and anti-resonant zero pairs after using proposed OAICS
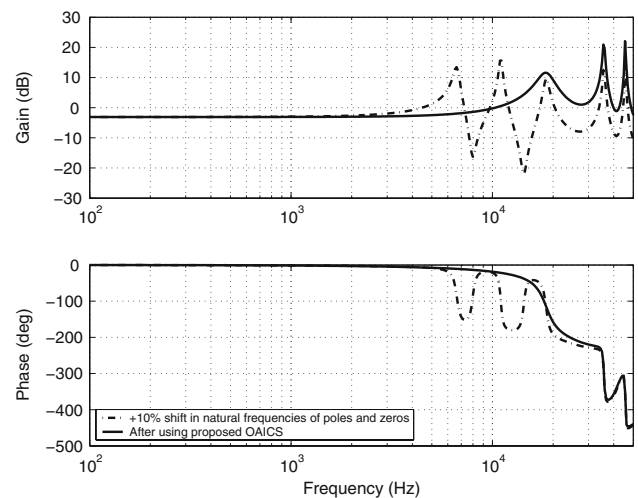
Fig. 9 Frequency response of $\tilde{P}^{-1}(z^{-1})P(z)$ with frequency variations of $+10\%$ in the first two resonant pole and anti-resonant zero pairs after using proposed OAICS

the natural frequencies of first two pair of minimum phase resonant pole and anti-resonant zero pairs of the PZT active suspension are perturbed by $\pm 10\%$. The frequency responses of the product of $\tilde{P}^{-1}(z^{-1})$ and $P(z)$ with -10 and $+10\%$ shifts in natural frequencies in the first two resonant pole and anti-resonant zero pairs after parametric convergence when using the proposed OAICS are shown in Figs. 8 and 9, respectively.

It can be seen from Figs. 8 and 9 that the proposed OAICS is effective in cancelling the minimum phase resonant pole and anti-resonant zero pairs using measured PES $y_m(k)$ solely, with no external excitation where white noise (or dither) is usually artificially introduced for broadband excitation in adaptive control applications.

For brevity but without loss of generality, the evolution of the parameters in $\mathbf{a}^T(N)$ and $\mathbf{b}^T(N)$ are not shown due to the large amount of coefficients. However, the parameters typically converge in less than 2s (corresponding to about 180 spindle rotations in a 5,400-rpm HDD) due to the conservative value of $\mu = 2.5 \times 10^{-4}$ chosen. It should be noted that the parametric convergence time can be improved greatly with a larger (but proper) choice of μ.

5.2 Experimental implementation

In this section, the proposed OAICS is verified with experiments implemented with the Φ-shaped PZT active suspension mounted on a VCM. The experimental setup is shown in Fig. 10.

For our experiments, the VCM with mounted PZT active suspension to be controlled is placed on a vibration isolation table. The proposed OAICS designed in Sect. 4 are implemented on the dSPACE digital control system using the DS 1103 PPC controller board with an onboard
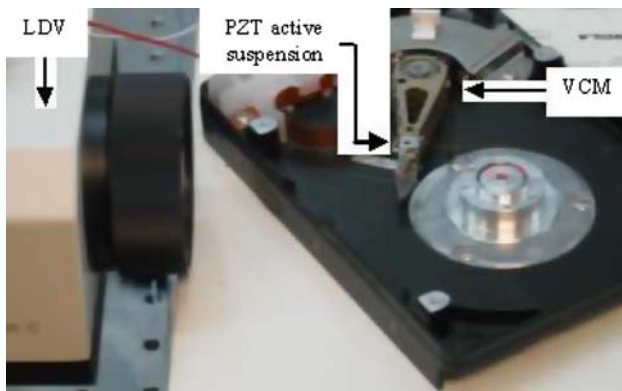
Fig. 10 Experimental setup showing the LDV displacement sensor with the PZT active suspension mounted on the VCM in a typical dual-stage configuration. The VCM is not actuated for our application of the OAICS

TM320F240 DSP as well as Analogue-to-Digital (A/D) and D/A converters of voltage limits at ±10 V for rapid digital controller prototyping. The digital controller's output from the OAICS are channelled to a PZT amplifier with a gain of twenty, which is then connected to the PZT elements in the Φ-shaped PZT active suspension for voltage actuation. The Polytec PSV-200 Scanning LDV (SLDV) measurement system is set to a single point measurement mode and is used as a displacement transducer to measure the displacement of the R/W head at the tip of the Φ-shaped PZT active suspension with a resolution of 0.5 μm/V.

5.2.1 Frequency responses

Using the proposed OAICS, the experimental frequency response of the open loop transfer function after parametric convergence is shown in Fig. 11. It can be seen that the desired gain crossover frequency of 2 kHz is achieved, with cancellation of the first two pairs of stable resonant pole and anti-resonant zero pairs hence enabling the PZT active suspension to behave like a pure gain up to a higher frequency range. This allows the Φ-shaped PZT active suspension to have a smaller inertia for faster error corrections at an extended frequency range.

The experimental frequency responses of sensitivity and complementary sensitivity transfer functions are shown in Fig. 12. It can be seen that a closed-loop bandwidth of about 2.7 kHz is achieved. This translates to more than one-third of the frequency of the first major resonant mode—where one-fifth is usually the norm achievable when using solely using digital notch filters to attenuate the gain of the resonant modes—of the Φ-shaped PZT active suspension, when compensation of the minimum phase anti-resonant zeros for a greater phase margin is implemented.
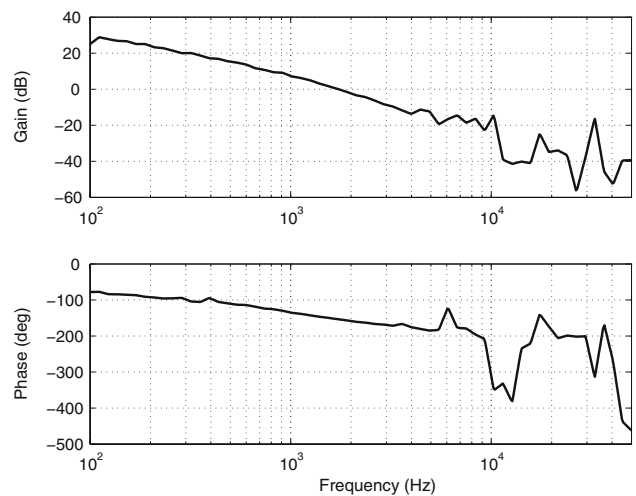

Fig. 11 Experimental frequency response of open loop transfer function. The first two dominant pairs of minimum phase resonant pole and anti-resonant zero are cancelled using the proposed OAICS with measured PES $y_m(k)$ only
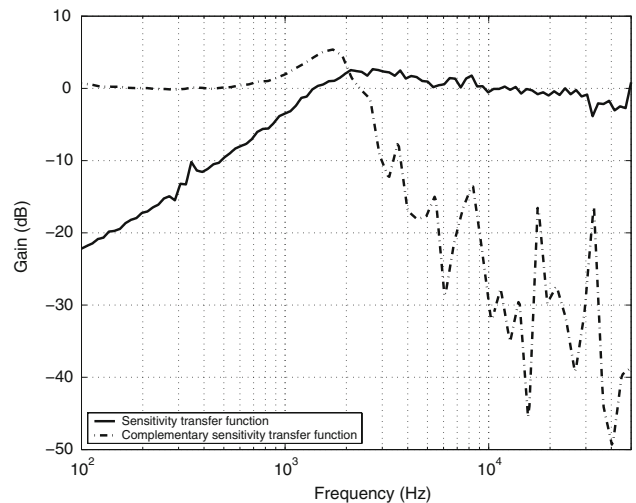

Fig. 12 Experimental frequency responses. *Solid* sensitivity transfer function. *Dashed-dot* complementary sensitivity transfer function

From Fig. 12, a low sensitivity after gain crossover frequency of less than 3 dB is achieved. The amplification of output disturbances at these frequencies where feedback control is degrading disturbance rejection is suppressed. Also, this ensures a low sensitivity when used in dual-stage HDD servo systems if the so-called Decoupled Master Slave (DMS) configuration is employed, which in essence is the product of sensitivities of the VCM loop and secondary actuator loop when using such a control topology (Pang et al. 2005).

5.2.2 Time response

To analyze the step response of the servo system, a series square wave of amplitude 0.25 V (corresponding to a
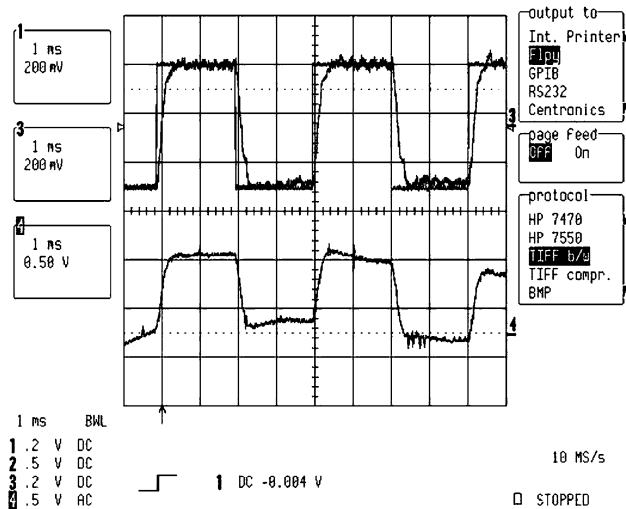
Fig. 13 Experimental step responses. *Top* reference and displacement of PZT active suspension at R/W head. *Bottom* control signal

short-span seek of 125 nm or several tracks in today's high end HDDs in either direction) is injected into the closed-loop system. The reference and step response of the Φ-shaped PZT active suspension measured using LDV as well as the corresponding control signal using proposed OAICS is shown in Fig. 13.

It should be noted that low frequency induced oscillations are caused by the measurement noise in the LDV system. It can seen from Fig. 13 that the experimental step response has a low overshoot (from larger phase margin), and the settling time is less than 0.5 ms. The control signal injected during adaptation when using the proposed OAICS is also kept at a low level of amplitude 0.4 V without saturating the Φ-shaped PZT active suspension.

6 Conclusion

In this paper, an online adaptive inverse control with saturation (OAICS) algorithm using measured position error signal (PES) is proposed to cancel the minimum phase resonant pole and anti-zero pairs in the PZT active suspension. Experimental results on a Φ-shaped PZT active suspension for usage in suspension-based dual-stage hard disk drives (HDDs) compensating the first two dominant stable pole-zero pairs achieve a high servo bandwidth (not possible with conventional digital notch filters) and a low positive sensitivity. Future works include improving the parametric updating laws to handle non-minimum phase zeros with faster convergence and applications to a dual-stage HDD.

References

Åström KJ, Hagander P, Sternby J (1984) Zeros of sampled systems. Automatica 20(1):31–38

Bjarnason E (1995) Analysis of the filtered-X LMS algorithm. IEEE Trans Speech Audio Process 3:504–514

Chen BM, Lee TH, Peng K, Venkataramanan V (2006) Hard disk drive servo systems, 2nd edn. Springer, New York

Chow JT, Lawrence DA (2001) Adaptive equalization for disk drives. In: Proceedings of the 2001 American control conference. Arlington, VA, pp 3836–3842

Du C, Zhang J, Guo G (2002) Vibration analysis and control design comparison of fluid bearing and ball bearing HDDs. In: Proceedings of the 2002 American control conference. Anchorage, AK, USA, pp 1380–1385

Eriksson LJ, Allie MC, Greiner RA (1987) The selection and application of an IIR adaptive filter for use in active sound attenuation. IEEE Trans Acoust Speech Signal Process. ASSP-35(4):433–437

Farhang-Boroujeny B (1998) Adaptive filters: theory and applications. Wiley, New York

Feintuch PL (1976) An adaptive recursive LMS filter. Proc IEEE 64:1622–1624

Kang C-I, Kim C-H (2005) An adaptive notch filter for suppressing mechanical resonance in high track density disk drives. Microsyst Technol 11(8–10):638–652

Ljung L (1977) Analysis of recursive stochastic algortihms. IEEE Trans Automat Control AC-22(4):551–575

Mosquera C, Gómez JA, Pérez F, Sobreira M (1999) Adaptive IIR filters for active noise control. In: Proceedings of sixth international congress on sound and vibration. Copenhagen, Denmark, pp 1571–1582

NHK Spring: Precision Springs and Components Division. http://info-sec.nhkspg.co.jp/eng/prod/disk.html (Online)

Pang CK, Wu D, Guo G, Chong TC, Wang Y (2005) Suppressing sensitivity hump in HDD dual-stage servo systems. Microsyst Technol 11(8–10):653–662

Pang CK, Guo G, Chen BM, Lee TH (2006) Self-sensing actuation for nanopositioning and active-mode damping in dual-stage HDDs. IEEE/ASME Trans Mechatron 11(3):328–338

Pang CK, Lewis FL, Ge SS, Guo G, Chen BM, Lee TH (2007a) Singular perturbation control for vibration rejection using the PZT active suspension as fast subsystem observer. IEEE Trans Ind Electron 54(3):1375–1386

Pang CK, Wong WE, Guo G, Chen BM, Lee TH (2007b) Nonrepeatable run-out rejection using online iterative control for high-density data storage. IEEE Trans Magn 43(5):2029–2037

Wang AK, Ren W (1999) Convergence analysis of the filtered-U algorithm for active noise control. Signal Processing 73:255–266

Widrow B, Walach E (1996) Adaptive inverse control. Prentice-Hall, Englewood Cliffs

Wu D, Guo G, Chong TC (2000) Adaptive compensation of microactuator resonance in hard disk drives. IEEE Trans Magn 36(5):2247–2250